Journal of Biomedical Optics

SPIEDigitalLibrary.org/jbo

Tumor glucose metabolism imaged *in vivo* in small animals with whole-body photoacoustic computed tomography

Muhammad Rameez Chatni
Jun Xia
Rebecca Sohn
Konstantin Maslov
Zijian Guo
Yu Zhang
Kun Wang
Younan Xia
Mark Anastasio
Jeffrey Arbeit
Lihong V. Wang

SPIE

Tumor glucose metabolism imaged *in vivo* in small animals with whole-body photoacoustic computed tomography

Muhammad Rameez Chatni,[a*] Jun Xia,[a*] Rebecca Sohn,[b] Konstantin Maslov,[a] Zijian Guo,[a] Yu Zhang,[c] Kun Wang,[a] Younan Xia,[c] Mark Anastasio,[a] Jeffrey Arbeit,[b] and Lihong V. Wang[a]
[a]Washington University in St. Louis, Department of Biomedical Engineering, St. Louis, Missouri 63130
[b]Washington University in St. Louis, Urology Division, Department of Surgery, St. Louis, Missouri 63110
[c]Georgia Institute of Technology and Emory University, Wallace H. Coulter Department of Biomedical Engineering, Atlanta, Georgia 30332

Abstract. With the increasing use of small animals for human disease studies, small-animal whole-body molecular imaging plays an important role in biomedical research. Currently, none of the existing imaging modalities can provide both anatomical and glucose molecular information, leading to higher costs of building dual-modality systems. Even with image co-registration, the spatial resolution of the molecular imaging modality is not improved. Utilizing a ring-shaped confocal photoacoustic computed tomography system, we demonstrate, for the first time, that both anatomy and glucose uptake can be imaged in a single modality. Anatomy was imaged with the endogenous hemoglobin contrast, and glucose metabolism was imaged with a near-infrared dye-labeled 2-deoxyglucose. [DOI: 10.1117/1.JBO.17.7.076012]

Keywords: acousto-optics; image analysis; photoacoustic spectroscopy.

Paper 12179 received Mar. 15, 2012; revised manuscript received Jun. 4, 2012; accepted for publication Jun. 6, 2012; published online Jul. 6, 2012.

1 Introduction

The importance of imaging tumor metabolism stems from the premise that anatomical changes alone are not an accurate metric for diagnosis, prognosis, and therapy. In particular, tumor metabolic imaging provides a spatial and temporal map of therapeutic response and guides treatment planning and selection. Therefore, simultaneous metabolic and anatomical imaging is very desirable and necessary not only in clinical settings but also in preclinical cancer models to improve our understanding of cancer, metastasis, and drug efficacy *in vivo*.[1–3]

Currently, X-ray computed tomography (CT)[4] and magnetic resonance imaging (MRI)[5] provide high-resolution anatomical images, but they cannot provide sufficient metabolic contrast without combining with metabolic imaging modalities, such as positron emission tomography (PET)[6] or single-photon emission computed tomography.[7] X-ray CT contrast agents based on iodine and barium only act as contrast enhancers.[4] Magnetic resonance spectroscopy (MRS) suffers from low sensitivity and resolution, and requires a high static magnetic field and a long imaging time (more than 1 h).[8] Despite the high cost of dual-modality imaging systems and the need for image registration,[9] metabolic imaging systems have their own limitations. Tumor metabolic imaging is based on the principle that cancer cells uptake more glucose than normal cells due to increased anaerobic glycolysis (the Warburg effect).[10] PET uses 18-F labeled fluorodeoxyglucose (FDG), a glucose analog, as a radioisotope for metabolic imaging.[6,11] While PET has high detection sensitivity, it is expensive; the radioisotopes are difficult to manufacture and have short half-lives.[12] In addition, the accumulated radiation dosage of the combined PET/CT may be carcinogenic and will confound experimental results in oncology, and thus cannot be ignored.[13–15] Hence, longitudinal monitoring of the same subject is usually not feasible. Pure optical imaging modalities, such as planar fluorescence imaging (PFI) and fluorescence optical tomography (FOT), have also been used to image tumor glucose metabolism with fluorophores conjugated to 2-deoxyglucose (2DG).[16] However, both PFI and FOT suffer from low spatial resolution and lack of intrinsic contrast, and have only been used to image tumor metabolism in superficial tumors.[16–19]

In this paper, we use a ring-shaped confocal photoacoustic computed tomography imaging system (RC-PACT)[20] to image both anatomy and tumor glucose metabolism at high spatial resolution in a single imaging modality. The system is based on the photoacoustic effect, where absorbed laser energy in tissue generates a local temperature rise, which is subsequently converted to pressure via thermoelastic expansion.[21] RC-PACT keeps the merits of optical imaging techniques, such as optical sensitivity and radiation safety, while providing high ultrasound-defined spatial resolution in optical quasi-diffusive and diffusive regimes with depth-to-resolution ratios of 100 or greater.[21] Additionally, multiple absorbers whose absorption spectra are different can be spectrally separated by varying the laser wavelengths.[21]

In RC-PACT, anatomical images were produced by endogenous hemoglobin contrast, and tumor glucose metabolism was imaged and quantified by spectrally separating the absorption of IRDye800-2DG[17] from that of hemoglobin. With the unique design of confocal free-space full-ring light illumination and full-ring ultrasound transducer array detection, our RC-PACT system generates *in vivo* cross-sectional images with simultaneous anatomical and metabolic assessments at high spatial resolution.

*These authors contributed equally to this work.

Address all correspondence to: Lihong V. Wang, Washington University in St. Louis, Department of Biomedical Engineering, St. Louis, Missouri 63130. E-mail: lhwang@biomed.wustl.edu

0091-3286/2012/$25.00

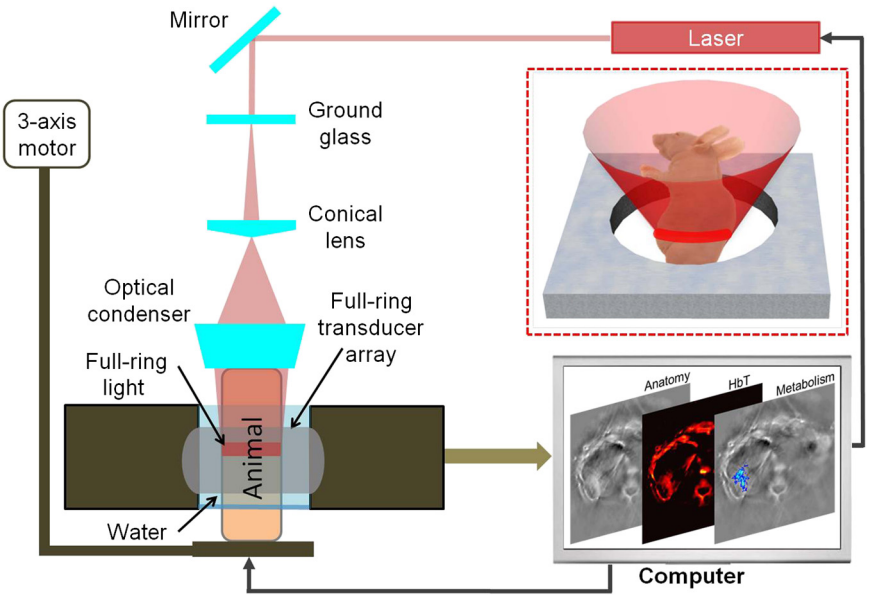

Fig. 1 Schematic of the full-ring confocal whole-body photoacoustic computed tomography (RC-PACT) system. The dashed box shows a three-dimensional view of the confocal design.

2 Methods

2.1 *RC-PACT Imaging System*

The schematic of the RC-PACT system[20] is shown in Fig. 1. A Ti-sapphire laser with the wavelength tunable from 690 to 990 nm was used as the excitation source. The laser beam passed through a conical lens and an optical condenser to form a light band around the animal. The maximum light intensity at the light band was approximately 15 mJ/cm^2, which was below the ANSI limit at the imaging wavelength.[22] The photoacoustic signals were detected by a 5 cm diameter full-ring transducer array custom built by Imasonic. The central frequency of the ultrasound transducer array is 5 MHz, and the bandwidth is 80% at the −6 dB point.[23] Signals from all 512 elements were amplified, selected by 64 8:1 multiplexers, and then digitalized by a 64-channel data acquisition system. The current system can acquire one frame of data per 1.6 s.

2.2 *Animal Preparation*

The animals were first anesthetized with isoflurane in pure oxygen using an isoflurane distribution unit (E-Z Anesthesia, Euthanex) and then mounted to the mouse holder using tape, with the forelegs attached to the top part of the animal holder and the hind legs attached to the bottom part. A tube was attached to the top part of the animal holder to deliver anesthesia gas. The body of the animal was immersed in a tank of water for acoustic coupling and surrounded by the full-ring ultrasound transducer array and sealed at the bottom by a flexible membrane.

For tumor glucose metabolism imaging experiments with IRDye800-2DG, the mice were made to fast for 6 hours to maximize the uptake of IRDye800-2DG in metabolically active cells.[17]

All experimental animal procedures were carried out in conformity with the guidelines of the US National Institutes of Health. The laboratory animal protocols for this work were approved by the Animal Studies Committee of Washington University in St. Louis.

2.3 *Image Reconstruction*

To account for the system's impulse response, the raw data was first deconvolved using the Wiener deconvolution. A modified back-projection algorithm, focal-line reconstruction,[24] was used for the *ex vivo* kidney imaging. The focal-line reconstruction algorithm accounts for the elevational focus of the arc-shaped transducer and renders images with better elevation resolution and signal-to-noise ratio (SNR).

For the spectral tumor imaging, the iterative half-time reconstruction algorithm[25] was used in order to generate accurate absorption values. The iterative reconstruction took 20 s per iteration on a 2.8 GHz processor.

2.4 *System Calibration*

In the spectral RC-PACT imaging experiments, the beam profile of the laser varied at different wavelengths, which led to changes in the fluence distribution, adding complexities on spectral separation. This problem can be solved either by aligning the optics after each wavelength tuning, which requires a tremendous amount of time in 3D scanning, or more efficiently, by compensating post-experiment. We used a phantom calibration method to compensate for both the laser power and the light band uniformity of different wavelengths. The phantom was made from a gelatin-water suspension mixed with 0.1% black ink. The suspension was filled in a cylindrical container, with inner diameter similar to the mouse cross-sectional diameter (20 mm), and was then cooled until gelled. The gelled phantom was then mounted on the RC-PACT imaging system and imaged using the same scheme as the animal experiment. Cross-sectional photoacoustic images of the phantom were reconstructed at each wavelength and the ring-shaped light variation was obtained based on the surface signal of the phantom image. The matrix of light variation was then used as a weighting function to calibrate the spectral *in vivo* images.

2.5 *Linear Least Squares Spectral Unmixing Algorithm*

The compensated photoacoustic image at each wavelength λ_i with spatial coordinates (x, y) in each cross-sectional slice was assumed to be dependent on the absorption of the endogenous hemoglobin and the exogenous IRDye800-2DG. This can be written as:

$$\mathrm{PA}(\lambda_i, x, y) = \varepsilon_{\mathrm{HbO}_2}(\lambda_i) C_{\mathrm{HbO}_2}(x, y) + \varepsilon_{\mathrm{Hb}}(\lambda_i) C_{\mathrm{Hb}}(x, y) + \varepsilon_{\mathrm{IRDye}}(\lambda_i) C_{\mathrm{IRDye}}(x, y),$$

where $\varepsilon_{\mathrm{HbO}_2}(\lambda_i)$, $\varepsilon_{\mathrm{Hb}}(\lambda_i)$ and $\varepsilon_{\mathrm{IRDye}}(\lambda_i)$ are the known molar absorption coefficients ($\mathrm{M}^{-1}\,\mathrm{cm}^{-1}$) of oxygenated hemoglobin, deoxygenated hemoglobin, and IRDye800-2DG at wavelength λ_i, respectively. $C_{\mathrm{HbO}_2}(x, y)$, $C_{\mathrm{Hb}}(x, y)$, and $C_{\mathrm{IRDye}}(x, y)$ are the molar (M) concentrations of oxygenated hemoglobin, deoxygenated hemoglobin, and IRDye800-2DG at location (x, y), respectively.

The relative concentrations of the three dominant absorbers were estimated by solving the set of linear equations using the linear least squares model with a constraint that the concentrations of any absorbers cannot be negative. Negative concentrations were set to zero.

$$\begin{bmatrix} C_{\mathrm{HbO}_2}(x, y) \\ C_{\mathrm{Hb}}(x, y) \\ C_{\mathrm{IRDye}}(x, y) \end{bmatrix} = (\varepsilon^T \varepsilon)^{-1} \varepsilon^T G,$$

where,

$$G = \begin{bmatrix} \mathrm{PA}(\lambda_1, x, y) \\ \mathrm{PA}(\lambda_2, x, y) \\ \mathrm{PA}(\lambda_3, x, y) \end{bmatrix} \quad \text{and}$$

$$\varepsilon = \begin{bmatrix} \varepsilon_{\mathrm{HbO}_2}(\lambda_1) & \varepsilon_{\mathrm{Hb}}(\lambda_1) & \varepsilon_{\mathrm{IRDye}}(\lambda_1) \\ \varepsilon_{\mathrm{HbO}_2}(\lambda_2) & \varepsilon_{\mathrm{Hb}}(\lambda_2) & \varepsilon_{\mathrm{IRDye}}(\lambda_2) \\ \varepsilon_{\mathrm{HbO}_2}(\lambda_3) & \varepsilon_{\mathrm{Hb}}(\lambda_3) & \varepsilon_{\mathrm{IRDye}}(\lambda_3) \end{bmatrix}.$$

The calculated concentrations have arbitrary units. Their ratios, however, are meaningful and can be used to estimate absolute concentrations. The total hemoglobin concentration (HbT) at each pixel is estimated by the following relationship:

$$\mathrm{HbT}(x, y) = C_{\mathrm{HbO}_2}(x, y) + C_{\mathrm{Hb}}(x, y).$$

Then the ratio of relative $\mathrm{HbT}(x, y)$ to IRDye800-2DG concentrations at each pixel was used to estimate the absolute concentrations of IRDye800-2DG *in vivo* for A431 and 786-O tumor mice images.

2.6 *Phantom Experiment for Absolute Concentration Estimation*

IRDye800-2DG (Licor Biosciences, USA) stock solution was prepared by dissolving 100 nanomoles in 1 mL sterile PBS buffer at pH 7.4. The stock solution was then diluted to IRDye800-2DG solutions at four different concentrations—16.7, 4.18, 1.11, and 0.55 μM, respectively. Each of these solutions and oxygenated bovine blood were loaded in five Silastic® tubes (Dow Corning, USA; inner diameter 0.3 mm; outer diameter 0.64 mm). These tubes were then glued to a 2 cm diameter gelatin cylinder.

3 Results

3.1 *Ex vivo Absolute Concentration Estimation*

The phantom was scanned by the RC-PACT imaging system at three wavelengths—776, 796, and 820 nm—to capture the absorption profile of IRDye800-2DG solution [(Fig. 2(a)]. The SNR of the signals from each of the tubes was calculated for the image acquired at 776 nm [Fig. 2(b)], by computing the

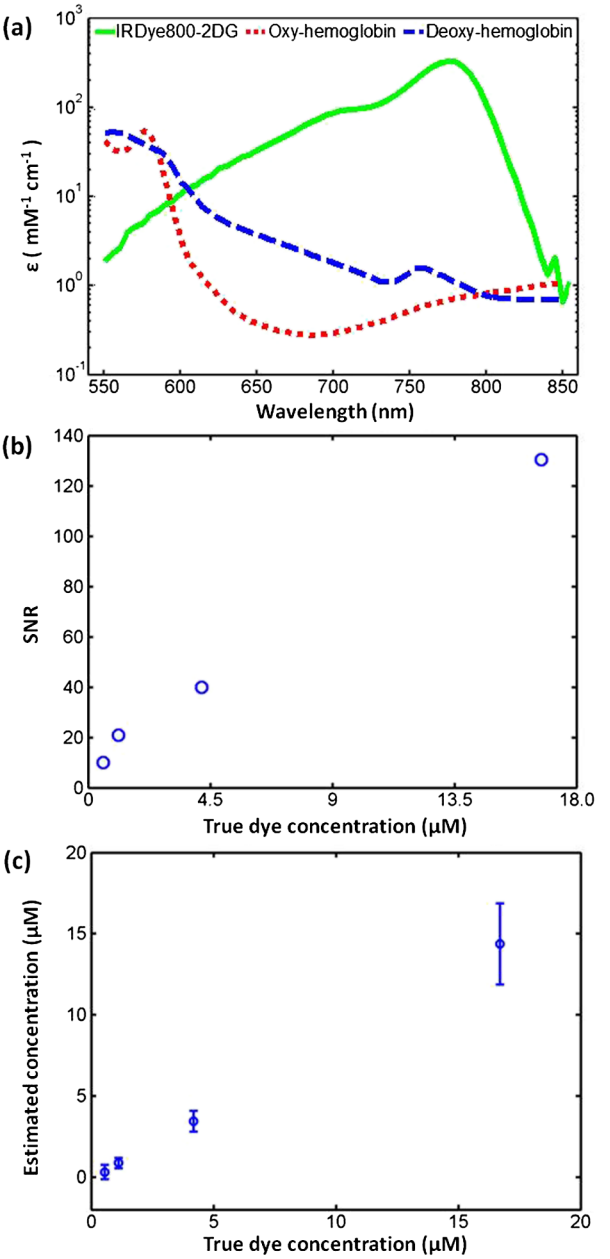

Fig. 2 (a) Molar absorption spectra of the two forms of hemoglobin and IRDye800-2DG. (b) SNR of RC-PACT signals from tubes containing IRDye800-2DG with different concentrations. (c) IRDye800-2DG concentrations in tubes estimated using the linear least squares spectral unmixing algorithm versus the actual concentrations.

ratio of the photoacoustic signals in the tube to the standard deviation of the background (the regions between the tubes).

The three RC-PACT images were reconstructed using the focal-line reconstruction algorithm,[24] and then compensated for wavelength-dependent laser power variation using the RC-PACT images of the ink phantom. Then these images were processed using a linear least squares spectral unmixing algorithm[26] to determine the relative concentrations of HbT and IRDye800-2DG in the five tubes. The HbT relative concentration image was scaled to 2.3 mM, and then the absolute concentration of each of the four IRDye800-2DG solutions was estimated. The predicted concentrations were averaged along each respective tube, and the mean and standard deviations calculated. Figure 2(c) shows the mean and standard deviation for each of the estimated IRDye800-2DG concentrations.

3.2 *Tumor Glucose Metabolism Imaging Using RC-PACT*

To investigate the *in vivo* capability of our system to simultaneously image anatomy and tumor metabolism, we imaged an athymic mouse bearing a subcutaneous xenografted A431 tumor. *In vivo* control RC-PACT images were acquired over an elevational distance of 10 mm with a 0.2-mm step size. At each elevational step, photoacoustic signals from all 512 transducers were acquired at three wavelengths—776, 796, and 820 nm. This served as a control experiment, since the dye was not injected.

Twenty-four hours after intravenous tail vein administration of 200 μL (0.4 mM) IRDye800-2DG solution, multispectral RC-PACT images were acquired using the same procedure as the control experiment. Tomographic inversion was performed to render images with a 0.05×0.05 mm^2 pixel size. The reconstructed images were then compensated for by RC-PACT images of a phantom for wavelength-dependent laser power and beam shape variations in the illumination ring.

Figure 3(a) shows a representative anatomical cross-section of the A431 tumor-bearing mouse acquired at 776 nm. Then the linear least squares unmixing algorithm was applied on every pixel of spectral RC-PACT images to calculate the relative HbT and IRDye800-2DG. The relative HbT concentrations were normalized by the maximum HbT concentration (observed in vena cava) and then scaled to 2.3 mM to recover the absolute concentration [Fig. 3(b)]. The absolute concentration of IRDye800-2DG at each pixel was then estimated by using the HbT concentration as a reference. After the experiment, the A431 tumor-bearing mouse was imaged using a lab-made fluorescence imager.

Figure 3(c) is an image of tumor glucose metabolism (IRDye800-2DG concentration map) overlaid on the gray-scale RC-PACT image acquired at 776 nm. The IRDye800-2DG concentration in the healthy skin area marked "HS" was used as the threshold for the image in Fig. 3(c). The uptake of IRDye800-2DG in the liver was nonuniform and twice as high as in the normal tissue, which agrees with the elevated expression of GLUT1 transporters in liver tissue.[17] The role of GLUT1 transporters in uptaking IRDye800-2DG has been investigated by competitive binding assays and dose-dependence experiments in a variety of tumor cell lines.[17] Despite the reported role of GLUT1 transporters,[17] the exact uptake mechanism of IRDye800-2DG may be different from that of FDG or native glucose due to differences in molecular size.

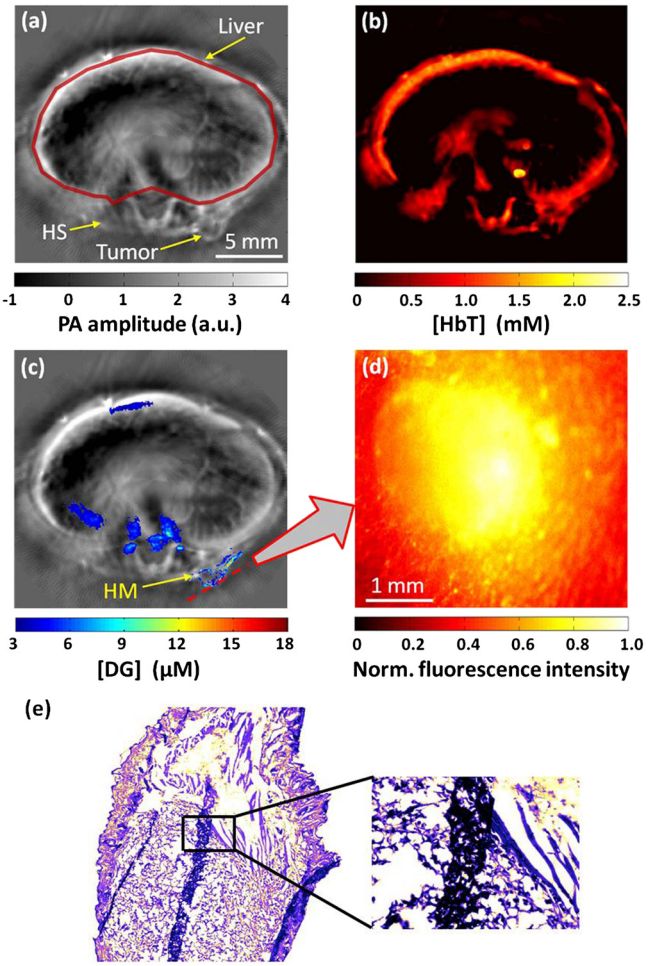

Fig. 3 *In vivo* images of an A431 tumor xenografted in the mouse skin. RC-PACT images of (a) the anatomy acquired at 776 nm (red boundary indicates the liver region), (b) HbT concentration (HbT), and (c) IRDye800-2DG concentration (DG) overlaid on the anatomical image. (d) *In vivo* fluorescence image of the cancerous skin, showing the IRDye800-2DG distribution. HS, the healthy skin; HM, hypermetabolic, (e) Hematoxylin and eosin stained histology image of the excised A431 tumor (Magnification: 4X). Magnified view showing A 431 tumor cells migrating into the muscle tissue interface (Magnification: 20X)

Elevated uptake of IRDye800-2DG at the outer tumor surface and inner skin-tumor interface was three times higher than that in the normal tissue in Fig. 3(c), indicating hypermetabolic (HM) activity. The RC-PACT imaging data also agreed with the fluorescence imaging results [Fig. 3(d)], which indicated a tumor-to-normal tissue contrast of approximately 3. The same image reconstruction and spectral separation methods were also applied on the control RC-PACT images, and no significant IRDye800-2DG uptake was observed.

As shown in Fig. 3(c), there is some uptake of IRDye800-2DG inside the tumor, but higher uptake is reflected at the tumor interfaces than in the tumor core. At least two explanations are possible (i) Based on the histology image in Fig. 3(e), the density of tumor cells in the tumor core is not very high. The comparatively lower uptake in this area may reflect the lower cell density. (ii) Figure 3(e) shows migrating tumor cells gathered at the muscle/tissue interface [inner interface in Fig. 3(c)]. These particularly active cells may have higher metabolic demand than cells in the core of the tumor. Therefore, the uptake may be higher at the interfacial boundaries.

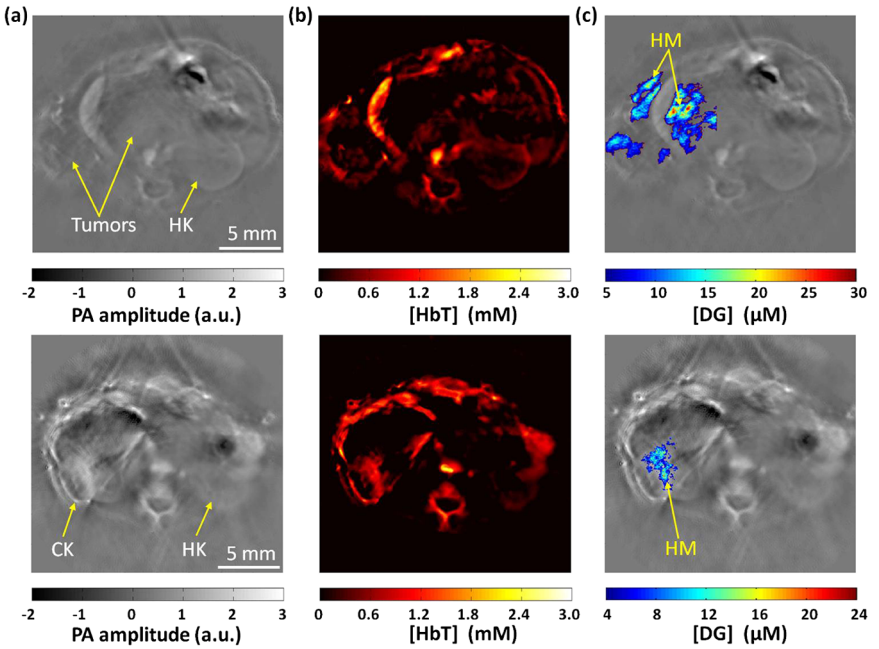

Fig. 4 *In vivo* RC-PACT images of orthotopically implanted 786-O kidney tumors. Top row: mouse 1. Bottom row: mouse 2. (a) Anatomical images acquired at 776 nm. (b) HbT concentration (HbT) images overlaid on the anatomical images. (c) IRDye800-2DG concentration (DG) images overlaid on the anatomical images. CK, cancerous kidney; HK, healthy kidney; HM, hypermetabolic.

To showcase the capability of our RC-PACT system to image the glucose metabolism of deeper tumors, we imaged two mice with orthotopically implanted 786-O tumor cells in their left kidneys. Following the control experiment, 200 μL of (0.4 mM) IRDye800-2DG was administered, and the mice were imaged after 24 h. This 24-h time window is sufficient for excess unbound IRDye800-2DG to be excreted by the kidneys and bladder. This also increases the likelihood that the imaged IRDye800-2DG reflects tumor glucose metabolism rather than the physical entrapment of excess IRDye800-2DG molecules within the tumor. After the *in vivo* experiment, the mice were sacrificed and the kidneys were excised for *ex vivo* RC-PACT imaging.

Figure 4(a) shows representative anatomical cross-sections of the two 786-O tumor-bearing mice. The linear least squares spectral unmixing algorithm was applied on the

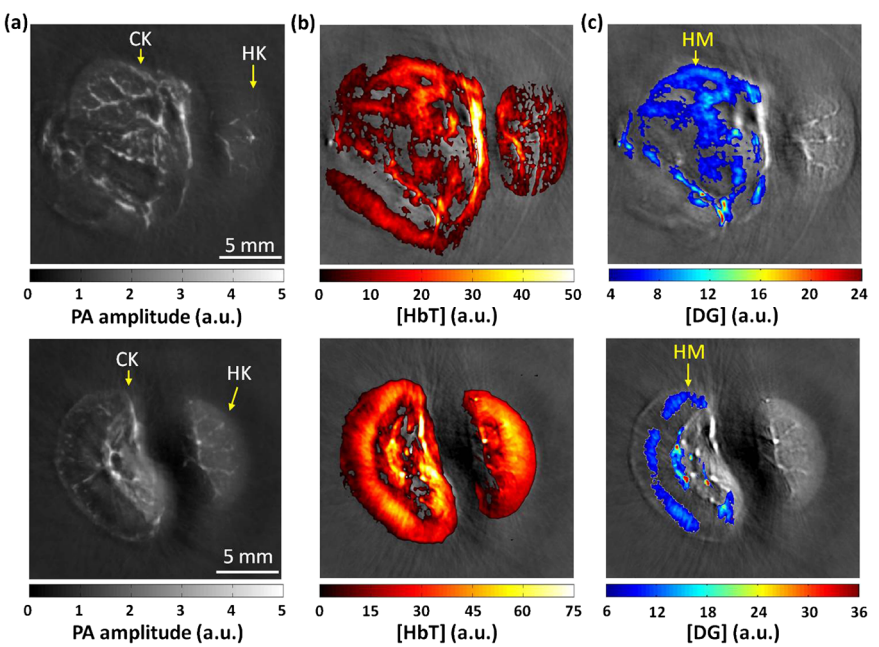

Fig. 5 *Ex vivo* RC-PACT images of freshly excised healthy and tumor bearing kidneys. Top row: mouse 1. Bottom row: mouse 2. (a) Maximum-amplitude-projection RC-PACT anatomical images acquired at 776 nm. (b) HbT concentration (HbT) images overlaid on the anatomical images acquired at the same cross-section. (c) IRDye800-2DG concentration [DG] images overlaid on the anatomical images acquired at the same cross-section. CK, cancerous kidney; HK, healthy kidney; HM, hypermetabolic.

multi-wavelength RC-PACT images, and relative concentrations of HbT and IRDye800-2DG were calculated. The HbT concentrations were normalized by the maximum HbT concentration (observed in vena cava), scaled to 2.3 mM [Fig. 4(b)], and then the absolute IRDye800-2DG concentrations in the anatomical cross-section were estimated.

Images of tumor glucose metabolism [Fig. 4(c)] were overlaid on the gray-scale PACT images acquired at 776 nm. In Fig. 4(c), the mean IRDye800-2DG concentration in healthy kidneys was used as the threshold to account for non-specific IRDye800-2DG uptake due to kidneys being the excretory route. The SNR for imaging IRDye800-2DG in the most metabolically active site in the tumor was 39.3 dB for mouse 1 and 38.3 dB for mouse 2. The tumor-to-normal tissue contrast for IRDye800-2DG uptake was approximately 3.3 at the most metabolically active site in the tumor. The same image reconstruction and spectral separation methods were also applied on the control RC-PACT images and no significant IRDye800-2DG uptake was observed.

3.3 *Ex vivo RC-PACT Imaging of Excised Kidneys*

Ex vivo experiments were performed using the top illumination scheme of RC-PACT The freshly excised kidneys were sealed in a gelatin phantom and scanned in the elevation direction. Multi-wavelength *ex vivo* RC-PACT images were reconstructed using the focal-line reconstruction algorithm.[24] The relative concentrations of HbT and IRDye800-2DG were determined by the linear least squares algorithm for every pixel. Figure 5(a) shows maximum-amplitude-projected images. Images of HbT [Fig. 5(b)] and IRDye800-2DG dye concentrations [Fig. 5(c)] are superimposed on the anatomical image acquired at 776 nm.

Figure 5 shows that endogenous hemoglobin contrast is present in both normal and tumor-bearing kidneys at similar concentrations. However, the tumor-bearing kidneys of both mice displayed higher IRDye800-2DG uptake than their normal counterparts. This uptake is not uniform in the tumors, possibly due to the differences in metabolic demand within the tumor mass. Additionally, necrotic tissue within the tumor may not uptake IRDye800-2DG. The average tumor-to-normal tissue contrast for excised kidneys of both mice was approximately 3.

4 Discussion

Molecular and anatomical imaging is of great importance due to its wide application in tumor biology, drug discovery, and early-stage cancer screening in both clinical and pre-clinical settings. In this report, we have demonstrated that RC-PACT provided tumor glucose metabolism and anatomic images with ultrasound-defined spatial resolution in a single imaging modality. While PET-CT and PET-MRI have been well established in the field,[3] RC-PACT is a promising and less expensive alternative with the advantages of non-ionizing laser radiation, non-radioactive optical contrast, and endogenous hemoglobin contrast. Additionally, image co-registration of anatomical and metabolic assessments is automatic.

Combined with spectral imaging,[27] RC-PACT also offers the possibility of resolving exogenous contrast agents, such as IRDye800-2DG. In tumor glucose metabolism imaging experiments, the wavelengths were selected to capture the steep changes in the absorption spectrum of IRDye800-2DG within a narrow spectral band of 40 nm. In this spectral region, the light scattering properties of the tissue are not expected to differ by more than 10% to 12%. Since the image contrast in photoacoustics is proportional to the product of absorption coefficient and local fluence, simple linear least squares spectral unmixing of multi-wavelength photoacoustic images may not be accurate in general. However, exceptions can be made when the chromophore to be resolved is surrounded by chromophores with relatively constant spectrum and/or are relatively weakly absorbing.[28] In our spectral range, the absorption of IRDye800-2DG declines rapidly as the wavelength increases, while the absorptions of oxy- and deoxy-hemoglobin are relatively unchanging. This absorption characteristic makes the linear least squares technique to be reasonable for resolving the IRDye800-2DG from background tissue hemoglobin absorption.[28] We tested the validity of our method of determining the absolute concentration of IRDye800-2DG using HbT by performing phantom experiments.

Besides imaging tumor glucose metabolism, RC-PACT can also benefit from near- infrared fluorescent dyes[29,30] for deep molecular imaging along with detailed, high resolution anatomical imaging. The possibility of multiplexing molecular imaging with anatomical imaging uniquely positions RC-PACT to have a broad impact in preclinical medical research and life sciences. In addition, as photoacoustic tomography has been extended to imaging biological tissue as deeply as 5 cm, RC-PACT holds the promise for molecular clinical imaging by scaling up the system for humans.

Acknowledgments

The authors appreciate Ms. Seema Dahlheimer's and Jim Ballard's close reading of the manuscript. This work was sponsored in part by National Institutes of Health grants R01 EB000712, R01 EB008085, R01 CA134539, U54 CA136398, R01 EB010049, R01 CA157277, and R01 CA159959. L. Wang has financial interests in Microphotoacoustics, Inc. and Endra, Inc., which, however, did not support this work.

References

1. M. Baker, "Whole-animal imaging: the whole picture," *Nature* **463**(7283), 977–980 (2010).
2. V. Koo, P. W. Hamilton, and K. Williamson, "Non-invasive in vivo imaging in small animal research," *Anal. Cell. Pathol.* **28**(4), 127–139 (2006).
3. R. A. de Kemp et al., "Small-animal molecular imaging methods," *J. Nucl. Med.* **51**(Suppl. 1), 18S–32S (2010).
4. D. W. Holdsworth and M. M. Thornton, "Micro-CT in small animal and specimen imaging," *Trends Biotechnol.* **20**(8), S34–S39 (2002).
5. H. Benveniste and S. Blackband, "MR microscopy and high resolution small animal MRI: applications in neuroscience research," *Prog. Neurobiol.* **67**(5), 393–420 (2002).
6. R. Myers, "The biological application of small animal PET imaging," *Nucl. Med. Biol.* **28**(5), 585–593 (2001).
7. A. G. Weisenberger et al., "SPECT-CT system for small animal imaging," *IEEE Trans. Nucl. Sci.* **50**(1), 74–79 (2003).
8. P. Meric et al., "In vivo 2D magnetic resonance spectroscopy of small animals," *Magn. Reson. Mater. Phys.* **17**(3), 317–338 (2004).
9. P. J. Slomka, "Software approach to merging molecular with anatomic information," *J. Nucl. Med.* **45**(Suppl. 1), 36S–45S (2004).
10. O. Warburg, "On the origin of cancer cells," *Science* **123**(3191), 309–314 (1956).
11. A. F. Chatziioannou, "Molecular imaging of small animals with dedicated PET tomographs," *Eur. J. Nucl. Med. Mol. Imag.* **29**(1), 98–114 (2002).
12. B. Morgan, "Opportunities and pitfalls of cancer imaging in clinical trials," *Nat. Rev. Clin. Oncol.* **8**(9), 517–527 (2011).
13. D. J. Brenner and E. J. Hall, "Computed tomography—an increasing source of radiation exposure," *New Engl. J. Med.* **357**(22), 2277–2284 (2007).

14. R. Fazel et al., "Exposure to low-dose ionizing radiation from medical imaging procedures," *New Engl. J. Med.* **361**(9), 849–857 (2009).
15. G. Brix et al., "Radiation exposure of patients undergoing whole-body dual-modality 18F-FDG PET/CT examinations," *J. Nucl. Med.* **46**(4), 608–613 (2005).
16. F. Leblond et al., "Pre-clinical whole-body fluorescence imaging: review of instruments, methods and applications," *J. Photochem. Photobiol. B: Biol.* **98**(1), 77–94 (2010).
17. J. L. Kovar et al., "Characterization and performance of a near-infrared 2-deoxyglucose optical imaging agent for mouse cancer models," *Anal. Biochem.* **384**(2), 254–262 (2009).
18. R. A. Sheth, L. Josephson, and U. Mahmood, "Evaluation and clinically relevant applications of a fluorescent imaging analog to fluorodeoxyglucose positron emission tomography," *J. Biomed. Opt.* **14**(6), 064014-064011-064018 (2009).
19. C. Q. Li et al., "Simultaneous PET and multispectral 3-dimensional fluorescence optical tomography imaging system," *J. Nucl. Med.* **52**(8), 1268–1275 (2011).
20. J. Xia et al., "Whole-body ring-shaped confocal photoacoustic computed tomography of small animals in vivo," *J. Biomed. Opt.* **17**(5), 050506 (2012).
21. L. V. Wang, "Multiscale photoacoustic microscopy and computed tomography," *Nat. Photon* **3**(9), 503–509 (2009).
22. American National Standard for the safe use of lasers, American National Standard Institute, New York (2000).
23. J. Gamelin et al., "A real-time photoacoustic tomography system for small animals," *Opt. Express* **17**(13), 10489–10498 (2009).
24. J. Xia et al., "Three-dimensional photoacoustic tomography based on the focal-line concept," *J. Biomed. Opt.* **16**(9), 090505 (2011).
25. M. A. Anastasio et al., "Half-time image reconstruction in thermoacoustic tomography," *IEEE Trans. Med. Imag.* **24**(2), 199–210 (2005)
26. J.-T. O. Meng-Lin Li et al., "Simultaneous molecular and hypoxia imaging of brain tumors in vivo using spectroscopic photoacoustic tomography," *Proc. IEEE* **96**(3), 481–490 (2008).
27. D. Razansky et al., "Multispectral opto-acoustic tomography of deep-seated fluorescent proteins in vivo," *Nat. Photon* **3**(7), 412–417 (2009).
28. P. Beard et al., "Quantitative photoacoustic imaging," in *Photoacoustic Imaging and Spectroscopy*, pp. 121–143, CRC Press, Baca Raton, FL (2009).
29. G. S. Filonov et al., "Bright and stable near-infrared fluorescent protein for in vivo imaging," *Nat. Biotech.* **29**(8), 757–761 (2011).
30. J. Lecoq and M. J. Schnitzer, "An infrared fluorescent protein for deeper imaging," *Nat. Biotech.* **29**(8), 715–716 (2011).